Analysis of Shape, Fluctuations, and Dynamics in Intermembrane Junctions

Lawrence C.-L. Lin,* Jay T. Groves,† and Frank L. H. Brown‡
*Department of Physics, and ‡Department of Chemistry and Biochemistry, University of California, Santa Barbara, California; and †Department of Chemistry, University of California, Berkeley, California

ABSTRACT A dynamic-elastic model for weakly adhered intermembrane junctions is presented. Helfrich membrane energetics coupled to hydrodynamic modes of the surrounding solvent reproduce the average shape, fluctuations, and dynamics of these junctions as measured experimentally. Comparison between numerical results and experimental data provides the first direct measure of surface tension in these systems (0.01–0.06 dyn/cm). The measurements suggest bilayer-bilayer adhesion energetics as the dominant source of surface tension in the experimental systems.

INTRODUCTION

Biology at the molecular, cellular, and organismal levels is critically dependent upon the structure, dynamics, and versatility of lipid bilayer membranes (1,2). In processes ranging from immunological response to cognitive function, intermembrane complexes between cells are crucial to normal biological function (3,4). Biologically, formation and stability of intercellular junctions are mediated by protein complexes at the cell surface, as well as the internal machinery of the cells involved. In vitro, lipid bilayers supported by solid substrates have become popular model systems for studying a wide range of related biological/biophysical structures and processes (5–7).

Recently, a class of model membrane systems with the potential to illuminate the properties of intermembrane junctions and related biological structures has been introduced (8,9). Giant unilamellar vesicles are ruptured over preexisting substrate-supported planar bilayers to create two closely adhered membranes. Two distinct adhesion states or intermembrane junctions can result from this process. So-called Type-1 junctions are characterized by an approximately uniform intermembrane spacing of a few nanometers. Adhesion spacing in the Type-1 geometry can be explained by the competition between attractive van der Waals forces and repulsive electrostatic and hydration potentials. In contrast, Type-2 junctions (see Fig. 1) are characterized by a much larger average intermembrane spacing of ~30–60 nm with adhesion provided by sparsely distributed, localized adhesion sites that affix the upper bilayer to the planar membrane underneath. The precise molecular nature of these random defects is not well understood; however, it is suspected that the defects (and hence the observed geometry of Type-2 systems) originate from imperfections in the solid-state support underlying the entire junction complex.

Type-2 junctions are especially promising for future biophysical studies—away from adhesion sites, the bilayers should not be strongly perturbed by the underlying support and may behave similarly to a free bilayer. Lateral diffusion within the upper bilayer, for example, is not adversely affected by the supporting matrix (8). Shape and transverse fluctuations of the upper bilayer in Type-2 junctions have also been measured to high resolution with fluorescence interference contrast (FLIC) microscopy (8,9), but a full analysis of this data has not previously been possible. Hence, it remains unverified that the bilayers in these systems are behaving completely as expected for a fluid bilayer sheet.

The difficulty in analyzing FLIC images of Type-2 junctions can be attributed to the irregular random geometries found in these systems. Any single point on the upper membrane surface is different from any other simply due to the geometry imposed by the localized adhesion sites. Similarly, any specific junction will be different from all others since adhesion geometry differs from junction to junction. It is necessary to properly model the geometry of each specific junction in question to quantitatively compare theory with experiment. Modeling the structure and dynamics of a membrane sheet in quasi-flat random geometries is not trivial and represents the main focus of this study.

In preliminary work (9) the above-mentioned problems were partially circumvented by analyzing only those portions of the junction far removed from all adhesion sites and assuming an artificial boundary condition around these regions for analysis purposes. Additionally, an ad hoc potential was introduced to enforce the intermembrane spacing and mean fluctuation amplitude. While this analysis did lead to interesting qualitative conclusions regarding the timescales for membrane fluctuation and relaxation, it was not possible to explain the overall junction shape or fluctuation amplitudes from a physical perspective. Furthermore, the many assumptions implicit in this analysis call into some question even the qualitative conclusions that were drawn.

Submitted June 21, 2006, and accepted for publication August 8, 2006.

Address reprint request to Frank L. H. Brown, Tel.: 805-893-5494; E-mail: flbrown@chem.ucsb.edu.

0006-3495/06/11/3600/07 $2.00

doi: 10.1529/biophysj.106.091843

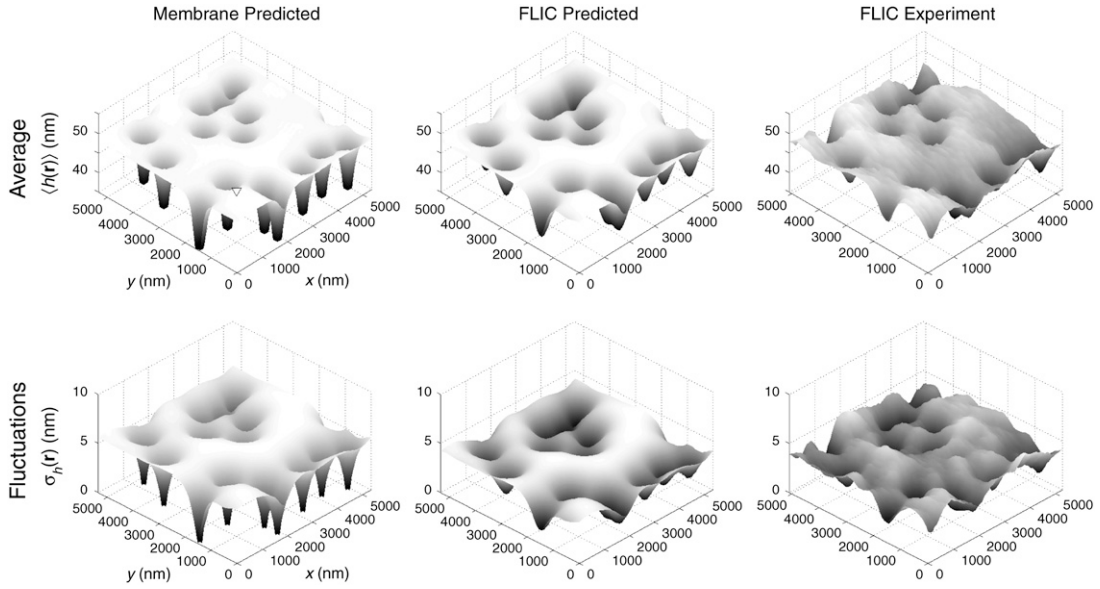

FIGURE 1 (*Top row*) Average bilayer shape for a representative configuration of pinning sites in a Type-2 intermembrane junction. The left panel displays the predicted average membrane shape $\langle h(\mathbf{r})\rangle$ assuming physical constants detailed in Table 1. The middle panel displays the predicted average FLIC image $\langle h_{\rm m}(\mathbf{r})\rangle$ corresponding to the same simulation. The right panel contains the experimental FLIC data (8). The triangle in the left image marks the location considered for dynamics as displayed in Fig. 2. (*Bottom row*) Analogous cases to the top row, but displaying fluctuations around the average $\sigma_{\rm h}^2(\mathbf{r})\equiv\langle h^2(\mathbf{r})\rangle - \langle h(\mathbf{r})\rangle^2$ and $\sigma_{\rm m}^2(\mathbf{r})\equiv\langle h_{\rm m}^2(\mathbf{r})\rangle - \langle h_{\rm m}(\mathbf{r})\rangle^2$. In all panels, the z-axis is expanded relative to x, y to emphasize detail. In this and subsequent figures, the value $\kappa = 7\times10^{-12}$ ergs is assumed.

This article reports calculations of bilayer structure and dynamic fluctuations within specific Type-2 junction geometries. We begin from a map of adhesion sites as inferred from the gross features of experimental data on particular Type-2 junctions. The average junction shape and fluctuation amplitudes are predicted on the basis of Helfrich energetics alone (without ad hoc potentials). Brownian dynamics incorporating the flow of water trapped between both bilayers leads to good agreement with experiment, both in terms of thermodynamic properties (junction shape and fluctuations) and dynamics. Quantitative agreement with experiment requires explicit consideration of the lateral resolution inherent to the FLIC microscopy technique and the nonvanishing surface tension present in adhered bilayers. By tuning the simulated surface tension to match experimental results, we deduce the magnitude of tension present experimentally. This study demonstrates the validity of a traditional elastic/hydrodynamic picture in modeling intermembrane junctions and demonstrates the extraction of elastic properties via direct comparison between detailed calculations and experimental data. In addition, this study serves as a starting point for understanding future experiments that take advantage of these promising model systems.

MODEL

Our model for Type-2 junctions assumes the lower bilayer to be a flat, impermeable wall at $z = 0$. The upper membrane lies above this plane and is parameterized by a height field $h(\mathbf{r})$ in the Monge gauge ($\mathbf{r} \equiv (x, y)$). The energetics are described by the Hamiltonian for a thin fluid sheet with bending elastic energy, surface tension, and an additional potential responsible for pinning the upper bilayer at the localized adhesion sites (10)

$$H = \int_{\rm A} d\mathbf{r}\left\{\frac{\kappa}{2}(\nabla^2 h(\mathbf{r}))^2 + \frac{\sigma}{2}(\nabla h(\mathbf{r}))^2 + \mathcal{H}_{\rm ad}[\,h(\mathbf{r})\,]\right\}. \quad (1)$$

Here, κ is the bending rigidity, σ is the surface tension, and $A = L^2$ is the area of our membrane patch projected onto the x,y plane. For computational purposes, we impose periodic boundary conditions in the x and y directions with period L. The above integral will always be evaluated with a short wavelength cutoff imposed by the lateral resolution of experiment ($\ell \sim 85$ nm)—i.e., we explicitly neglect structure not amenable to experimental determination, which allows for numerical calculations despite the large physical size (microns in linear dimension) of the available FLIC microscopy images.

We assume the upper membrane is directly attached to the flat lower bilayer over adhesion regions $<\ell$ in diameter (below, we find this assumption completely consistent with the available experimental data). We model specific Type-2 junctions starting from an experimental FLIC image and identifying the clearly apparent adhesion sites (see Fig. 1). Denoting the (x, y) position of adhesion site i by $R_{\rm i}$, we treat each site identically as a conical defect in the upper bilayer, with $h(\mathbf{R}_{\rm i}) = 0$ and a coarse-grained slope, s, describing the contact angle of the pin. Mathematically, we enforce these defects through a series of strong harmonic constraints at the points $R_{\rm i}$ and the nearest neighbors to $R_{\rm i}$ in our discrete representation of the x, y plane. Explicitly, for a junction with N adhesion sites

$$\begin{aligned}\mathcal{H}_{\rm ad}[h(\mathbf{r})] &= \sum_{\rm i=1}^{\rm N}\mathcal{H}_{\rm pin}([h(\mathbf{r})],\mathbf{R}_{\rm i})\\ \mathcal{H}_{\rm pin}([h(\mathbf{r})],\mathbf{R}_{\rm i}) &= \frac{\gamma}{2}h(r)^2\delta(\mathbf{r}-\mathbf{R}_{\rm i})\\ &\quad + \frac{\gamma}{2}\sum_{\rm n.n.}[h(\mathbf{r}) - s\ell]^2\delta(\mathbf{r}-\mathbf{R}_{\rm i_{n.n.}}), \quad (2)\end{aligned}$$

where γ determines the strength of the pinning and *n.n.* refers to the four nearest neighbors to position $\mathbf{R}_i$ corresponding to translation of $\pm\ell$ in both the x and y directions. In what follows, s is chosen to best fit the experimental data. The quantity γ is simply chosen large enough to ensure the membrane is well localized (i.e., further increasing γ does not alter the reported results).

Membrane dynamics are specified by a nonlocal Langevin equation, including the effects of Stokes flow in the surrounding solvent (11,12)

$$\frac{\partial h(\mathbf{r},t)}{\partial t} = \int_{-\infty}^{\infty} d\mathbf{r}'\, \Lambda(\mathbf{r}-\mathbf{r}')[F(\mathbf{r}',t)+\zeta(\mathbf{r}',t)], \qquad (3)$$

where $F(\mathbf{r}, t) = -\delta H/\delta h(\mathbf{r}, t)$ is the force per area on the membrane, $\Lambda(\mathbf{r}-\mathbf{r}')$ is the hydrodynamic interaction kernel, and $\zeta(\mathbf{r}, t)$ represents the (Gaussian, white) thermal noise in the system with average magnitude dictated by the fluctuation-dissipation theorem at temperature T. The form of the hydrodynamic kernel depends upon the fluid environment surrounding the membrane and will be discussed further below. Although Eq. 3 is expected to break down at wavelengths comparable to bilayer thickness (13), it should be entirely adequate for the wavelengths considered herein.

Our simulations were carried out using the harmonic Fourier Space Brownian Dynamics (FSBD) algorithm. Neglecting technical details that are described elsewhere (14,15), we simply note that Eqs. 1 and 3 reflect a harmonic system, albeit a somewhat complex one. The equations of motion can be rewritten in terms of a set of completely decoupled eigenmodes. Once the eigenmodes are known, it is a simple matter to compute the average membrane shape, local variance around this average, and associated time-correlation functions for direct comparison to experimental data. The bulk of numerical calculations come down to the identification of the normal modes via matrix diagonalization. (In our numerical analysis we consider regions with $L/\ell = 64$. A region of this size implies $64 \times 64 = 4096$ modes in the system, requiring the diagonalization of a full 4096×4096 matrix.)

Expressions for the hydrodynamic kernel $\Lambda(r)$ are derived using the Stokes equations for an incompressible fluid and boundary conditions specific to the geometry of interest. We present here $\Lambda_{\mathbf{k}}$, the Fourier-transformed kernels applied in the FSBD calculations. Commonly, the membrane is assumed to reside in an infinite, unbounded fluid, which results in the solution (11)

$$\Lambda_{\mathbf{k}}^{\text{inf}} = \frac{1}{4\eta k}, \qquad (4)$$

where η is the viscosity of the surrounding fluid. In the case of intermembrane junctions, however, the lower bilayer and supporting matrix act as a confining wall, impermeable to solvent flow. The additional requirement of incompressibility in the plane of the membrane yields a solution (15,16)

$$\Lambda_{\mathbf{k}}^{\text{conf}} = \Lambda_{\mathbf{k}}^{\text{inf}} \frac{e^{2kd} + e^{-2kd} - 2[1+2(kd)^2]}{e^{2kd} - [1+2(kd)^2] + 2kd}, \qquad (5)$$

where d is the average distance from the membrane to the wall. A slightly different form can result if boundary conditions at the membrane surface are handled differently (17). All results reported here assume Eq. 5.

We point out that Eq. 5 (unlike Eq. 4) is equal to zero when $k = 0$, implying that the zero wavevector mode does not evolve in time. The volume of fluid trapped between upper and lower bilayers in our system is directly proportional to the $k = 0$ system mode and is therefore also constant. (Higher k modes do not affect the volume because their sinusoidal behavior integrates to zero over the box.) The condition of solvent incompressibility coupled with the geometry of our system naturally insures that trapped solvent volume is strictly conserved in our calculations.

COMPARISON TO EXPERIMENT

The preceding considerations outline the machinery necessary to predict junction thermal and dynamic properties as a function of the physical constants (κ, σ, s, η, T) and specific geometry of pinning sites present in individual junction complexes. The parameters used in our simulations are collected in Table 1 and the results of our simulations for a specific Type-2 junction are presented in Fig. 1. While κ, η, and T are known from experiment, the pinning slope and surface tension of the system have not previously been reported. The values of these two constants were inferred by simultaneously fitting our calculations to both the average bilayer shape and shape fluctuations. The range of σ and s presented in Table 1 reflect the determined best-fit values for a series of nine different regions extracted from the experimental data.

Table 1 presents two possible values for the membrane-bending modulus. The expression $\kappa = 7 \times 10^{-12}$ ergs reflects the value obtained by a crude (unpublished) analysis of the experimental data (Y. Kaizuka, University of California, Berkeley, 2004, personal communication). Since this value is somewhat larger than typically expected for fluid lipid bilayers and cannot be quantitatively accurate, we have also considered a value of $\kappa = 1 \times 10^{-12}$ ergs in the analysis described below. We stress from the outset that the precise value of κ used in our numerics does not significantly alter our results. We comment further on this point below.

In fitting experimental data we account for the fact that FLIC microscopy images necessarily reflect local averaging of true bilayer shape over the point spread function, $G(\mathbf{r})$, of the instrument. The essential physics of this effect is captured by

$$h_{\text{m}}(\mathbf{r},t) = \int_{-\infty}^{\infty} d\mathbf{r}'\, G(\mathbf{r}-\mathbf{r}')h(\mathbf{r}',t) \qquad (6)$$

where $h_{\text{m}}(\mathbf{r}, t)$ is the experimentally measured height at position $\mathbf{r}$, reflecting a local average of the true membrane

TABLE 1 Model parameters used in and inferred from numerics

Parameter	Description	Value	Reference
κ	Bending modulus	7×10^{-12} ergs	*
		(1×10^{-12} ergs)	†
σ	Surface tension	0.011–0.052 dyn/cm	‡
		(0.021–0.058 dyn/cm)	§
s	Pinning slope	0.11–0.26	‡
		(0.21–0.39)	§
η	Solvent viscosity	0.01 poise	Water
T	Temperature	20°C	¶
L	System size	5.432 μm	¶
ℓ	Lattice spacing	84.88 nm	¶
γ	Pinning constant	10^8 ergs cm^{-2}	‖

The values of σ and s are extracted as best-fit values to reproduce experimental data in each of the nine independent ~5 μm × 5 μm regions studied. The reported range of values reflects differences in the individual regions. The specific region displayed in Fig. 1 yields $\sigma = 0.038$ dyn/cm and $s = 0.26$ assuming $\kappa = 7 \times 10^{-12}$ ergs.

*Personal communication with Y. Kaizuka.

†Alternate value for κ for comparison purposes.

‡Best fit to data of Kaizuka and Groves (8) assuming $\kappa = 7 \times 10^{-12}$ ergs.

§Best fit to data of Kaizuka and Groves (8) assuming $\kappa = 1 \times 10^{-12}$ ergs.

¶Kaizuka and Groves (8).

‖Sufficiently large so that increasing the value does not change the results.

geometry in this vicinity. For numerical convenience, we use a Gaussian approximation to the point spread function with variance $(190\ \text{nm})^2$ appropriate for the wavelength of light used in experiment (18). Since the FSBD algorithm is formulated in Fourier space, the convolution of Eq. 6 is readily handled as a simple multiplication; expressions for $h_m(\mathbf{r}, t)$ averages, variance, and correlation functions are derived with little additional complication beyond the analogous quantities for $h(\mathbf{r}, t)$. Fitting to experiment was accomplished using the following procedure. Trial values of s and σ were used to calculate average bilayer shape $\langle h_m(\mathbf{r})\rangle$ and fluctuations $\sigma_m(\mathbf{r}) \equiv \sqrt{\langle h_m^2(\mathbf{r})\rangle - \langle h_m(\mathbf{r})\rangle^2}$ for direct comparison to the experimental data in each of the considered nine regions. The procedure was iterated over a range of s- and σ-values to identify the closest fit for each region. Across the different regions, the obtained values of the surface tension and slope spanned $s = 0.11$–0.26 (0.21–0.39) and $\sigma = 0.011$–0.052 dyn/cm (0.021–0.058 dyn/cm) for $\kappa = 7 \times 10^{-12}$ ergs (1×10^{-12} ergs). For the specific example shown in Fig. 1, the procedure yielded $s = 0.26$ and $\sigma = 0.038$ dyn/cm with the reported significant figures indicating the allowed interval of variation for trial parameter values.

In principle, the above convolution procedure is approximate. The exact procedure used to infer the FLIC image, $h_m(\mathbf{r})$, from $h(\mathbf{r})$ is quite involved (18,19) with potential quantitative deviations from Eq. 6. In practice, we verified that Eq. 6 worked well for a variety of test cases with varying membrane geometries (deviations between approximate and exact treatments for h_m differ by $\sim$0.5 nm away from the pinning sites and $<$2 nm near the pinning sites). Using Eq. 6 has the advantage of numerical efficiency and given its near perfect agreement with the full procedure provides a convenient means to generate in silico FLIC images. Thermal averaging can be carried out analytically, thus avoiding the computationally prohibitive task of averaging over thermal configurations and repeating this process for all parameter values.

The images in Fig. 1 demonstrate a close correspondence between simulation and experiment. Both in this particular data set and the other eight analyzed, the parameters most relevant to overall membrane shape are the bending rigidity, κ, and the pinning slope, s. Although we take κ as a known quantity and only vary s in our fitting procedure, it should be emphasized that κ for this system is not precisely determined by experiment (8,9). It happens that we find equally good fits to membrane shape using different κ-values, $(0.5$–$7.0) \times 10^{-12}$ergs, while allowing s to adjust to a new local minimum, so our analysis cannot shed any light on the value of the bending rigidity for these systems. Although the value of the minimized s is altered somewhat by the chosen value for κ (see Table 1), these differences do not manifest themselves in the convolved images in a significant way. Any reasonable κ-value yields a unique predicted slope at contact, but all pairs of κ and correspondingly minimized s fit the experimental FLIC data equally well. For this reason, it is not sensible to simultaneously fit the experimental data to an expanded set of physical constants (κ,s,σ); there are an essentially infinite number of equally good solutions. Fortunately, various choices for κ have only slight impact on the extracted surface tension values. Hence, we can obtain an estimate for σ despite our ignorance of the precise value for the bending rigidity. The physical basis for the insensitivity of our results on κ is twofold. First, the convolution inherent to FLIC measurements obscures details around the pinning site, which are sensitive to κ and s individually (as opposed to the larger-scale features, which are only sensitive to the κ, s pair). Secondly, the fluctuations are dominated by surface tension in these systems. In principle, our analysis could be used to extract κ if it were the case that σ were orders-of-magnitude smaller than observed.

It is interesting to note that the true membrane shape is quite a bit more flat (away from pins) than suggested by the FLIC images, a consequence of the pinning sites influencing $h_m(\mathbf{r})$ over the range of the point spread function. The FLIC convolution also explains the relatively shallow experimentally observed pinning depth. The experimental data is completely consistent with an upper membrane pinned on the flat substrate below. The observed depth of $\sim$5–10 nm can be explained purely as a result of the point spread function. Within our simulations, the average membrane height is dictated by the local geometry around pinning sites, the density of pins in a particular image, and the bending rigidity of the bilayer. We reiterate that our simulations were carried out in a periodic geometry, while experimental images reflect a portion of junction embedded in a larger surface. Consequently, there are some unavoidable deviations between simulation and experiment due to our artificial handling of boundary conditions. (These deviations are most pronounced near the boundary of the regions under consideration. The differences between theory and experiment in Fig. 1 are actually somewhat overemphasized, since region boundaries are clearly apparent and tend to attract the eye.)

Surface tension manifests itself most strongly in the maximum magnitude of fluctuations. However, s, κ, and $G(\mathbf{r})$ also influence the overall shape of the fluctuation images seen in the lower panels of Fig. 1. The surface tensions we extract from the experimental data ($\sigma = 0.011$–0.058 dyn/cm) are approximately an order-of-magnitude smaller than seen in Type-1 junctions (20), but considerably larger than typical tensions in unilamellar vesicles ($\sim 10^{-4}$ dyn/cm) (21). Interestingly, the range of σ-values we extract from experiment fall exactly within the window of values expected for bilayer-bilayer adhesion energy densities (22) ($W_{ad} \sim 10^{-2} - 10^{-1}$ dyn/cm). This fact suggests that the tension in Type-2 junctions results from an attraction between lipids in the upper bilayer and the supported bilayer below. While the pinning geometry and bending rigidity of the bilayer make it energetically unfavorable for the bilayer to satisfy this attraction by flattening out into a global Type-1

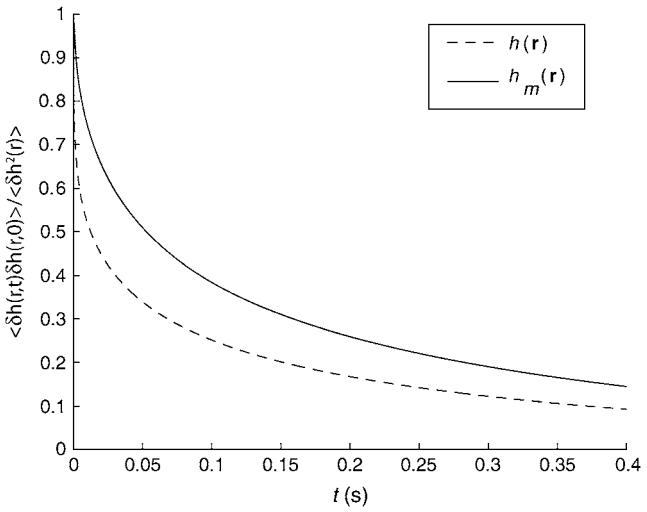

FIGURE 2 Plot of a typical time-correlation functions $\langle \delta h(\mathbf{r},t)\delta h(\mathbf{r},0)\rangle$, where $\delta h(\mathbf{r},t) \equiv h(\mathbf{r},t) - \langle h(\mathbf{r})\rangle$, without the convolution over $G(\mathbf{r})$ (*dashed line*) or $\delta h(\mathbf{r},t) \equiv h_{\mathrm{m}}(\mathbf{r},t) - \langle h_{\mathrm{m}}(\mathbf{r})\rangle$, with the convolution over $G(\mathbf{r})$ (*solid line*). This particular decay reflects measurement at the point indicated by the triangle in the upper-left plot in Fig. 1.

geometry, it is possible for lipids to favorably interact with the lower bilayer sheet at points where the two bilayers converge (either in a distant region of Type-1 adhesion or in local structures around the pinning sites). These regions of local membrane-membrane interaction can serve as lipid reservoirs (23), from which excess area in the upper sheet is created at the expense of removing lipids from their adhered state. Removing an area of bilayer, a, from such an adhered reservoir to create fluctuations in the junction carries an energetic cost of aW_{ad}. Inclusion of such an area-dependent term in the system Hamiltonian naturally leads to W_{ad} as the measured surface tension for the junction.

In addition to thermal averages, the present simulation methodology is capable of modeling junction dynamics. In Fig. 2, we plot a typical time-correlation function for the height of the upper bilayer at a particular point in space. As is the case for the thermal properties, averaging over the point spread function leads to quantitative deviation from the true behavior of the membrane. The point spread function effectively quenches short wavelength undulations, which are the fastest modes of the system. The predicted FLIC data hence shows a slower initial decay than does the raw height data. In agreement with prior arguments (9) we find the inclusion of confined hydrodynamics is essential to predicting reasonable relaxation times. The free hydrodynamic kernel of Eq. 4 results in timescales that are several orders-of-magnitude too fast relative to experiment (with or without FLIC averaging), while the results plotted in Fig. 2 are consistent with experimental findings.

While the present results potentially represent a considerable improvement over previous modeling efforts (9), current experiments are not precise enough to fully validate or refute our findings in the context of system dynamics. As in all fluorescence-based methodologies, FLIC is limited by the finite lifetime of the dyes used in the measurement. From a practical standpoint, this limits the time course of membrane fluctuation measurements to $<$20 s. Unfortunately, the relevant timescales involved are on the order of tenths of a second to seconds, meaning that even the longest experimental measurements provide insufficient data to infer well-converged correlation functions.

To make this point explicit, in Fig. 3, we show the error bars associated with the extraction of height fluctuation correlations from a data set of finite length. Unlike other results presented in this work, the data in this figure was collected by explicitly running Brownian dynamics trajectories as described in Lin and Brown (14). (The methodology is similar to the traditional ''Brownian dynamics with hydrodynamic interactions'' (24), but takes advantage of the harmonic nature of our potentials to allow for time steps of arbitrary length.) In each pane of Fig. 3 we ran 100 identical numerical experiments for the duration specified (τ). The circles represent the correlation function extracted using the full ($100 \times \tau$ in length) data set, whereas the error bars reflect the variance in the averages associated with averaging only over the individual length τ blocks. Current experiments are roughly comparable to the situation displayed in the leftmost pane of the figure and this degree of uncertainty can be seen in the actual experimental data. (The results presented in (9) reflect further averaging over many locations on the membrane surface to calculate a reasonably converged result at

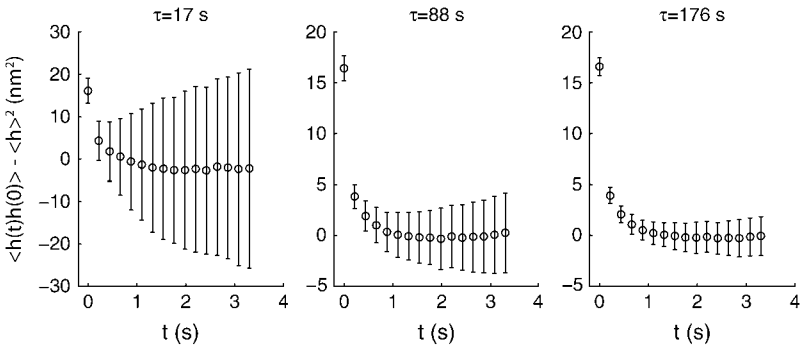

FIGURE 3 Plot of the average correlation function $\langle h(t)h(0)\rangle - \langle h\rangle^2$ and variance in this average, assuming results are extracted from a finite data set of duration $\tau \sim 17$s, $\tau \sim 88$ s, and $\tau \sim 176$ s for the left, middle, and right panels, respectively. The results here reflect the time correlations at the point indicated in the upper-left plot in Fig. 1.

the expense of losing all detail associated with a particular position within the junction). The other two panes show how the situation could be dramatically improved if averaging an additional 5–10 times longer were possible. At present, it is not possible to validate the details of Eq. 5, and in particular not the specific d dependence, due to the limited duration of the data streams. As already mentioned, however, the slowing of dynamics implied by the presence of the wall some tens of nanometers below the membrane is certainly qualitatively confirmed by experiment.

DISCUSSION

The complex geometries observed in Type-2 intermembrane junctions are not amenable to direct analytical analysis, yet the time and length scales involved are well suited to a traditional elastic/hydrodynamic treatment of the problem. The FSBD approach applied herein (14,25) seems ideally suited to the analysis of these systems and has allowed for extraction of information from experiment that would otherwise have been difficult. The combined approach of FLIC measurement and detailed FSBD analysis allows us to measure and suggest a source for the surface tension in intermembrane junctions. Additionally, the approach suggests a geometry for the pinning sites in these structures and points out the limitations of currently available data sets with regard to extracting dynamical information.

We have not attempted to rationalize the extracted values for the slope, s, surrounding the adhesive pinning sites in our model. Experimentally, the pins are immobile and persist over a range of conditions (8). These observations suggest that pinning defects originate from imperfections in the underlying solid supporting matrix, but the microscopic structure of such defects remains poorly understood. Given the physical ambiguity surrounding pinning in Type-2 junctions, we have modeled the interactions by way of a simple adjustable geometric constraint. The slopes we infer may seem large to some readers, but we note that even more extreme geometries have been attained in other bilayer systems (26,27).

The computational approach presented in this work explicitly considers the system geometry to perform a customized mode analysis specific to the geometrical nuances of each specific experiment. While we have discussed thermal fluctuations in model membrane systems here, our strategy can just as easily be applied to estimate membrane motions in more complex cellular environments with nonthermal energy sources (28). The FSBD scheme we present is potentially well suited to studying a very broad class of biophysical systems. The primary limitation at present appears to be the limited availability of detailed experimental data (such as the FLIC data considered here) for direct comparison.

This study highlights some general properties of membrane systems that likely influence a wide range of biophysical properties at the cell surface. As demonstrated by Fig. 1, the detailed geometry of membrane surfaces strongly influences bilayer fluctuations. This will be true whether bilayer geometry is imposed by pinning to a solid support or is mediated by intercellular protein complexes. In the case of intercellular junctions, the interplay between membrane geometry and fluctuations has the potential to affect protein binding and dissociation kinetics. As the initial complex is formed membrane geometry is altered, which will influence subsequent binding events. Similarly, the hydrodynamics of a volume of water bound between two bilayers is significantly different from the case of a single isolated bilayer. The implied slowing of membrane fluctuations and relaxation as modeled here should also influence intercellular binding kinetics.

We thank Y. Kaizuka and R. Parthasarathy for helpful discussions and providing us with their experimental data.

This work was supported by the National Science Foundation (grants No. CHE-0349196 and No. CHE-0321368). F. B. is an Alfred P. Sloan research fellow.

REFERENCES

1. Lodish, H., D. Baltimore, A. Berk, S. L. Zipursky, P. Matsudaira, and J. Darnell. 1995. Molecular Cell Biology, 3rd Ed. Scientific American Books, New York.
2. Sackmann, E. 1995. Biological membranes architecture and function. *In* Structure and Dynamics of Membranes: Part A. From Cells to Vesicles. Elsevier Science, Amsterdam, The Netherlands.
3. Grakoui, A., S. K. Bromley, C. Sumen, M. M. Davis, A. S. Shaw, P. M. Allen, and M. L. Dustin. 1999. The immunological synapse: a molecular machine controlling T-cell activation. *Science*. 285: 221–227.
4. Qi, S. Y., J. T. Groves, and A. K. Chakraborty. 2001. Synaptic pattern formation during cellular recognition. *Proc. Natl. Acad. Sci. USA*. 98:6548–6553.
5. Brian, A., and H. M. McConnell. 1984. Allogeneic stimulation of cytotoxic t cells by supported planar membranes. *Proc. Natl. Acad. Sci. USA*. 81:6159–6163.
6. Sackmann, E. 1996. Supported membranes: scientific and practical applications. *Science*. 271:43–48.
7. Sackmann, E., and M. Tanaka. 2000. Supported membranes on soft polymer cushions: fabrication, characterization, and applications. *Trends Biotechnol*. 18:58–64.
8. Kaizuka, Y., and J. T. Groves. 2004. Structure and dynamics of supported intermembrane junctions. *Biophys. J*. 86:905–912.
9. Kaizuka, Y., and J. T. Groves. 2006. Hydrodynamic damping of membrane thermal fluctuations near surfaces imaged by fluorescence interference microscopy. *Phys. Rev. Lett*. 96:118101.
10. Helfrich, W. 1973. Elastic properties of lipid bilayers: theory and possible experiments. *Z. Naturforsch*. 28c:693–703.
11. Granek, R. 1997. From semi-flexible polymers to membranes: anomalous diffusion and reptation. *J. Phys. II* (*Paris*). 7:1761–1788.
12. Doi, M., and S. F. Edwards. 1986. The Theory of Polymer Dynamics. Clarendon Press, Oxford.
13. Shkulipa, S. A., W. K. den Otter, and W. J. Briels. 2006. Simulations of membrane dynamics at intermediate length scales. *Phys. Rev. Lett*. 96:178302.
14. Lin, L. C.-L., and F. L. H. Brown. 2004. Dynamics of pinned membranes with application to protein diffusion on the surface of red blood cells. *Biophys. J*. 86:764–780.
15. Lin, L. C.-L., and F. L. H. Brown. 2006. Simulating membrane dynamics in nonhomogeneous hydrodynamic environments. *J. Chem. Theory Comput*. 2:472–483.

16. Seifert, U. 1994. Dynamics of a bound membrane. *Phys. Rev. E.* 49: 3124–3127.

17. Gov, N., A. G. Zilman, and S. A. Safran. 2004. Hydrodynamics of confined membranes. *Phys. Rev. E.* 70:011104.

18. Parthasarathy, R., B. L. Jackson, T. L. Lowery, A. P. Wong, and J. T. Groves. 2004. Nonequilibrium adhesion patterns at lipid bilayer junctions. *J. Phys. Chem. B.* 108:649–657.

19. Parthasarathy, R., and J. T. Groves. 2004. Optical techniques for imaging membrane topography. *Cell Biochem. Biophys.* 41: 391–414.

20. Daillant, J., E. Bellet-Amalric, A. Braslau, T. Charitat, G. Fragneto, F. Graner, S. Mora, F. Rieutord, and B. Stidder. 2005. Structure and fluctuations of a single floating lipid bilayer. *Proc. Natl. Acad. Sci. USA.* 102:11639–11644.

21. Pecreaux, J., H.-G. Dobereiner, J. Prost, J.-F. Joanny, and P. Bassereau. 2004. Refined contour analysis of giant unilamellar vesicles. *Eur. Phys. J. E.* 13:277–290.

22. Boal, D. 2002. Mechanics of the Cell. Cambridge University Press, Cambridge.

23. Brochard, F., P. G. DeGennes, and P. Pfeuty. 1976. Surface tension and deformations of membrane structures: relation to two-dimensional phase transitions. *J. Phys.* (*Paris*). 37:1099–1104.

24. Ermak, D. L., and J. A. McCammon. 1978. Brownian dynamics with hydrodynamic interactions. *J. Chem. Phys.* 69:1352–1360.

25. Lin, L. C.-L., and F. L. H. Brown. 2004. Brownian dynamics in Fourier space: membrane simulations over long length and time scales. *Phys. Rev. Lett.* 93:256001.

26. Bar-Ziv, R., R. Menes, E. Moses, and S. A. Safran. 1995. Local unbinding of pinched membranes. *Phys. Rev. Lett.* 75:3356–3359.

27. Karlsson, R., A. Karlsson, and O. Orwar. 2003. A nanofluidic switching device. *J. Am. Chem. Soc.* 125:8442–8443.

28. Lin, L. C.-L., N. Gov, and F. L. H. Brown. 2006. Nonequilibrium membrane fluctuations driven by active proteins. *J. Chem. Phys.* 124: 074903-1–074903-15.